Mechanics of Pressure-Adaptive Honeycomb

Roelof Vos, Ron Barrett and Albert Romkes

Journal of Intelligent Material Systems and Structures 2011 22: 1041 originally published online 1 August 2011
DOI: 10.1177/1045389X11412638

Mechanics of Pressure-Adaptive Honeycomb

ROELOF VOS,[1,*] RON BARRETT[2] AND ALBERT ROMKES[3]

[1]*Faculty of Aerospace Engineering, Delft University of Technology, The Netherlands*

[2]*Department of Aerospace Engineering, The University of Kansas, USA*

[3]*Department of Mechanical Engineering, The University of Kansas, USA*

ABSTRACT: Pressure-adaptive honeycomb is a new type of adaptive structure that can exhibit great strains by relying on a pressure differential to alter the structural stiffness. The structure consists of a grid of honeycomb cells that extend a significant length perpendicular to the plain of the hexagons. Each cell possesses a pouch that can be pressurized and alter the stiffness of the structure. An analytical model is presented that predicts the stress–strain behavior in principal directions of this pressure-adaptive honeycomb. The predictions of the analytical model are shown to correlate well to experimental tests on a 130-cell aluminum honeycomb specimen that is loaded up to compressive strains of 12.5%. Based on this model, an equivalent material stiffness is defined for the honeycomb cell walls that can be employed in a FEA. An FE approximation of a 145-cell honeycomb beam based on this equivalent material stiffness is shown to correlate well to experimental results of a three-point bend test of such a specimen. The model of equivalent material stiffness greatly reduces the complexity of the FE approximation by eliminating the need to define a pouch or an internal pressure field. Therefore, the prediction method could be used in a design tool for pressure-adaptive honeycomb structures.

Key Words: actuator, morphing, autonomic structures, cellular, inflatable.

INTRODUCTION

For more than a century, aircraft have benefitted from changes in wing geometry to account for variable flight conditions or for flight control. Although early incarnations of continuous wing deformation were quickly replaced by discrete high-lift devices and hinged control surfaces, a renewed interest in wing morphing has resulted in new implementations of this relatively old technology. In the 1980s, the mission adaptive wing explored the effectiveness of continuous leading and trailing edge deformation. This wing had an internal mechanism to flex the outer wing skin and produce a symmetrical section for supersonic speeds, a supercritical section for transonic speeds, and a high-camber section for subsonic speeds. Flight tests demonstrated that an improvement in lift-to-drag ratio of 20% could be obtained in large parts of the flight envelope, while some parts even showed an increase of 100% (Gould, 1981; DeCamp and Hardy, 1984; Lewis et al., 1990; Powers and Webb, 1997). Even though the flight tests demonstrated advantages of wing morphing, there were significant drawbacks to the way the morphing was achieved. Bulky, heavy hydraulic screw jacks were employed to induce the deformation in the wing. In addition, internal mechanisms employing multiple linkages ensured the desired kinematics of the mechanism. This resulted in a complex actuation system. As with so many wing morphing mechanisms, comparatively small, powerful actuators imparted forces and motions to small sections which were then distributed to the larger surface. The weight increments associated with such a system clearly proved prohibitive.

Other, contemporary endeavors are under way in military aircraft, where wing morphing is applied to satisfy various mission requirements such as loiter and high-speed dash. One morphing concept relies on the simultaneous change in wing sweep, aspect ratio and span (Figure 1(a)). This is achieved by a scissor-link mechanism inside the wing in combination with an elastic skin (Flanagan et al., 2007; Bowman et al., 2007). Another morphing concept folds part of the wing against the side of the fuselage, such as to reduce the total wetted area of the wing during high-speed dash (Figure 1(b)). In the latter approach, the wing hinges are locally covered with a flexible membrane wing skin (Ivanco et al., 2007; Love et al., 2007). Both of these morphing concepts have been tested in the wind tunnel and have demonstrated promising results. One of the main drawbacks for both concepts is the level of complexity that is

*Author to whom correspondence should be addressed.
E-mail: r.vos@tudelft.nl
Figures 1, 2 and 7–9 appear in color online: http://jim.sagepub.com

1045-389X/11/10 1041–15 $10.00/0 DOI: 10.1177/1045389X11412638

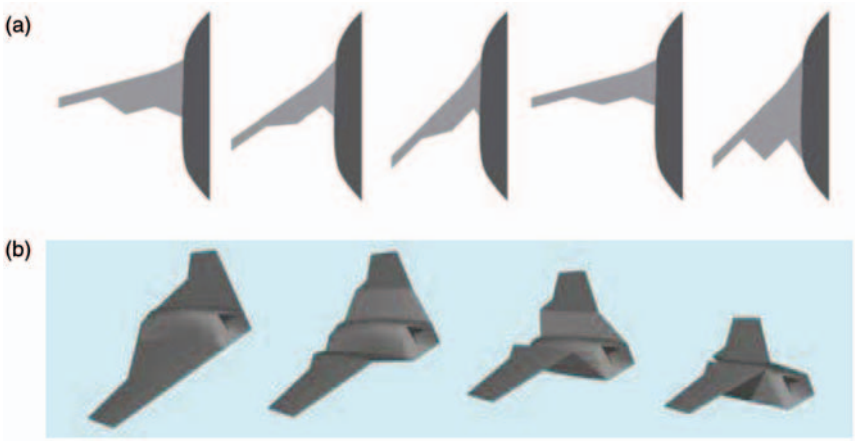

Figure 1. *Morphing concepts. (a) Morphing wing congurations for high-lift, climb, cruise, loiter, and maneuver (Bowman et al., 2007). (b) Lockheed Martin baseline morphing concept (Love et al., 2007).*

required to achieve wing morphing. For instance, the scissor-link structure consists of a complicated mechanism of hinging spars and ribs that are all interconnected. The folding wing requires individual hinges at the root and mid-span of the wing that must be able to carry the wing bending moment. In addition to the added complexity, this also must add considerable weight to an otherwise relatively lightweight wing structure.

In an effort to reduce the complexity of the morphing wing system, adaptive actuators were introduced to actively change (part of) the wing structure. The DARPA smart wing program utilized shape-memory-alloy (SMA) wires and torque tubes to induce various wing deformations, such as local trailing edge camber, to optimize the spanwise twist distribution (Sanders et al., 2004; Martin et al., 2004). In 2005, Boeing introduced a higher level of adaptivity when it flew its SMA-actuated chevrons. These chevrons, designed to reduce noise levels during take-off and landing, were slightly bent into the exhaust of the engine. At elevated altitude, the decreasing local temperature caused the SMA actuators to deform such that the chevrons opened up, increasing the efficiency of the engine (Calkins and Butler, 2006) Even though this demonstrated the effectiveness of SMA actuators in civil aircraft structures, application of adaptive materials in primary and secondary structures is still prohibited due to the lack of a documented material database.

Because of the restricted use of smart materials in primary and secondary aircraft structures, a new type of adaptive structure based on ordinary honeycomb cells was developed. In this article, it is shown that by pressurizing honeycomb cells, their stiffness can be altered, which can subsequently be used to induce large structural deformations. The best way of explaining the mechanics of this structure is by considering Figure 2. The test article presented in this figure consists of 23 honeycomb cells, each occupied with an airtight pouch. The cells extent a significant length (30 cm) with respect to the plane of the honeycomb cells. When deflated (Figure 2(a)), the stiffness of the honeycomb is relatively low, such that the external load (in the form of a weight) compresses the structure. By increasing the pressure in each of the pouches, the stiffness of the structure increases dramatically. This results in a structure that, under the external load, displays only little deformation. In other words, altering the pressure can alter the external geometry of this structure.

This pressure-adaptive honeycomb can be implemented in aerospace structures to locally change curvatures of components. It can be manufactured from conventional aerospace materials such as steel or aluminum and the pouches can be manufactured from an aerospace-grade of nylon. The pressurization of the pouches can be done by relying on bleed air from the compressor (in case of a jet engine) or by using the exhaust manifold pressure (in case of a reciprocating engine). Alternatively, the pouches can be filled with a fixed amount of air, after which they are totally sealed. In that case, the altitude–pressure relation is used as a stimulus to induce structural deformations in the pressure-adaptive honeycomb. The latter option has a higher degree of adaptivity, on par with Boeing's variable chevrons in terms of total actuation energy density (both estimated to be on the order of 10 kJ/kg, Anon., 2009; Vos and Barrett, 2010). The major differences are that all the materials in the pressure-adaptive honeycomb are immediately certifiable to FAR 23 and FAR 25 standards, they cost orders of magnitude less than SMA's and they are integrated as distributed actuators resisting distributed forces, rather than point actuators needing heavy, complicated motion distribution mechanisms. An example application where gross local camber changes of an airfoil were induced by pressure-adaptive honeycomb was shown by Vos and Barrett (2010).

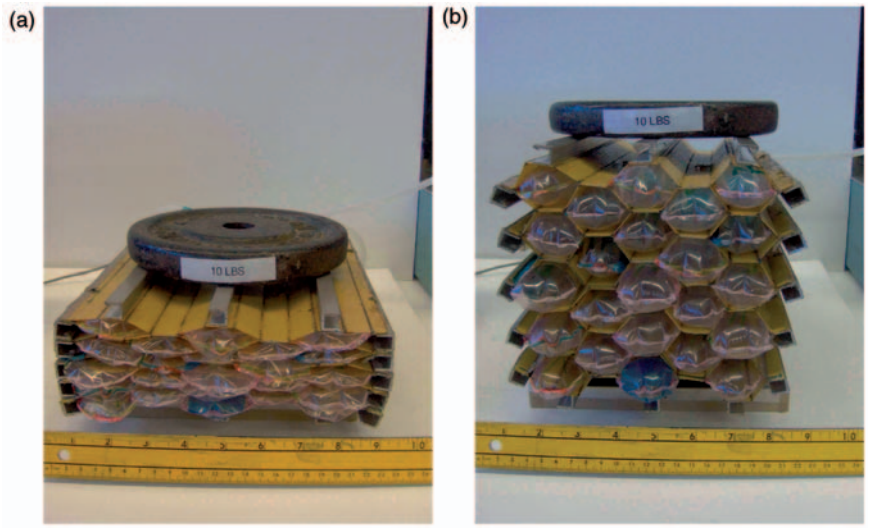

Figure 2. *Proof-of-concept pressure-adaptive honeycomb structure. (a) Deflated pouches. (b) Inflated pouches.*

Conventional inflatable structures have been around for several decades and have proven their applicability in aerospace structures (Cadogan et al., 2004; Norris and Pulliam, 2009). Partial inflation of individual cells on inflatable wings has been shown to alter airfoil geometry and change the aerodynamic characteristics (Reinhard et al., 2001). The only pneumatic actuator that could be qualified as an adaptive structure is a pneumatic artificial muscle that was designed to actuate a flap system (Woods et al., 2008). The load-bearing capacity of honeycomb was shown for a rigidified inflatable structure. It was shown that three-dimensional honeycomb blocks could be inflated and subsequently rigidified to form walls for residential buildings. It was shown that these structures yielded low-material usage, a short-manufacture time, and the ability to easily build complex structures (Khire et al., 2006). Other applications of (non-pressurized) honeycomb have included energy absorption under in-plane compressive loading (Atli and Gandhi, 2008). Adaptive honeycomb has also been investigated where honeycombs made from SMA were used to enhance the energy absorption capability of honeycomb (Shaw et al., 2007). Finally, honeycomb has been successfully used in adaptive skins that enable wing morphing (Bubert et al., 2010; Olympio and Gandhi, 2010). Even though all these research efforts have similarities to this invention, they all differ substantially from the fundamental concept that is presented in this article.

In the following sections, a mathematical representation of the pressurized honeycomb structure is presented. An equivalent model is derived that can be used in a finite element (FE) approximation of this structure instead of the complex interaction of pouch and honeycomb wall. Such a model can, in turn, be employed when a pressure-adaptive structure is embedded in a conventional wing structure. A step-by-step approach is taken in the development of this model, such that the results of each step could be verified against experimental results.

MODELING PRESSURIZED HONEYCOMB

To model the properties of an entire pressurized honeycomb grid, it is convenient to consider the smallest repeating unit and determine its properties. Such an incremental unit can be extracted from a regular honeycomb grid by finding the symmetry planes within the honeycomb structure. In Figure 3, the incremental unit that forms the basis of this model is extracted from a honeycomb grid. This incremental unit is a rectangle that measures $l(1+\cos\ \theta)$ in width and l sin θ in height, where θ is termed the honeycomb angle ($\theta = \pi/3$ in Figure 3) and l the length of each of the honeycomb faces. The thickness-to-length ratio (t/l) is a dimensionless characteristic of honeycombs and will appear frequently in this article.

The objective of this section is to define an equivalent material stiffness of the honeycomb cells that incorporates both the stiffness of the material and the pressure-induced stiffness. This has the advantage that the complexity of a geometric model that is used for the FE calculations can be significantly reduced. If this simplification is used, there is no need to explicitly define each of the pouches that occupy most of the volume in each cell. In addition, the pressure loading due to the pressurized volume can be absent. The equivalent stiffness can be perceived as an artificial stiffness that is assigned to the honeycomb walls such that the stiffness that is induced by the pressurized pouches is accounted for, while keeping the kinematic properties of the

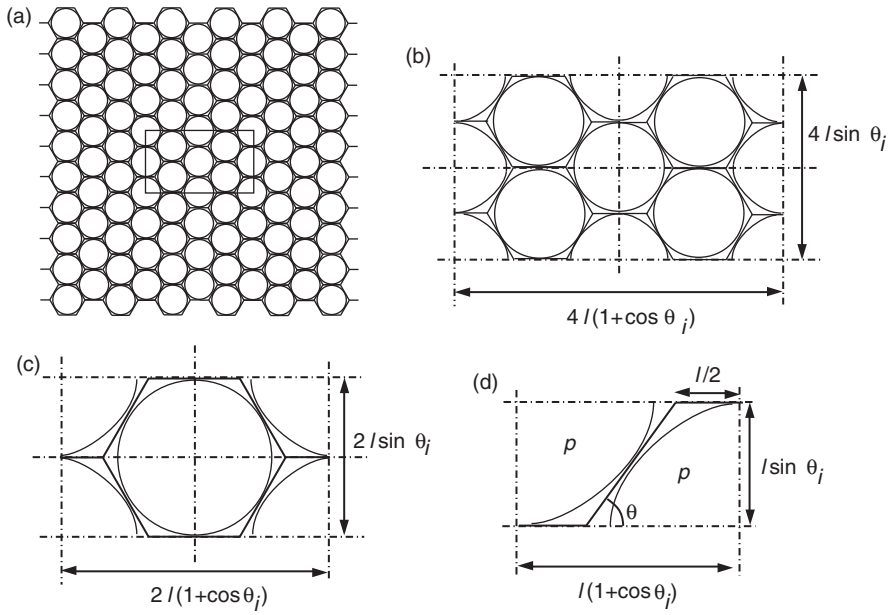

Figure 3. *Breakdown of honeycomb grid into incremental units. (a) Full honeycomb grid. (b) Rectangular section with symmetry lines. (c) Single cell with pouch. (d) Incremental unit; basis for model.*

honeycomb unaltered. In a mathematical sense, the equivalent material stiffness E^{eq} is the sum of the Young's modulus of the material, E^m, and the pressure-induced modulus, E^p:

$$E^{eq} = E^m + E^p \tag{1}$$

In the subsequent sections, a model is presented to obtain the pressure-induced modulus, E^p.

Cellular Material Theory for Honeycombs

Cellular material theory (CMT) relies on a Newtonian approach to relate the overall stiffness of a honeycomb block to the characteristics of the honeycomb geometry and material, i.e. t/l, θ_i, and E^m. This theory is explicitly explained in Gibson and Ashby (1988) and is used in this analysis in the reverse direction in that the overall characteristics of pressurized honeycombs are already known (from experimental testing) and the *equivalent* material stiffness is to be determined.

To relate the material stiffness, and the geometry to the overall stiffness of the structure, the reader is asked to consider Figure 4. It can be shown that when a honeycomb cell is loaded solely in the longitudinal (x) direction, the deformation occurs only in the diagonal walls of the section. One of those walls is considered in Figure 4 and it is shown how the wall forms an s-shape, such that the wall angle, θ_i at the corners remains constant, which is in accordance with extensive observations of deforming honeycomb cells.

The longitudinal force that is introduced at either end of the diagonal wall can be related to the stress in the horizontal direction *via* the honeycomb angle:

$$F_x = \sigma_x l \sin\theta_i. \tag{2}$$

Due to equilibrium, the moment can be defined as:

$$M = \frac{F_x l \sin\theta_i}{2}. \tag{3}$$

Using Euler–Bernoulli beam theory, the beam deflection, δ, can be related to the moment according to:

$$\delta = \frac{F_x l^3 \sin\theta_i}{E^m I}, \tag{4}$$

where E^m is the material stiffness and I the second moment of area which reads $I = t^3/12$ for a wall of uniform thickness and unit width. The resulting strain in the x-direction can be found from the projection of δ onto the horizontal axis:

$$\varepsilon_x = \frac{\delta \sin\theta_i}{l(\cos\theta_i + 1)} = \frac{\sigma_x l^3 \sin^3\theta_i}{12EI(\cos\theta_i + 1)}. \tag{5}$$

The resulting equivalent stiffness of the honeycomb structure, $\bar{E}_x^m = \sigma_x/\varepsilon_x$, follows from the previous derivation (Gibson and Ashby, 1988):

$$\bar{E}_x^m = E^m \left(\frac{t}{l}\right)^3 \frac{\cos\theta_i + 1}{\sin^3\theta_i}. \tag{6}$$

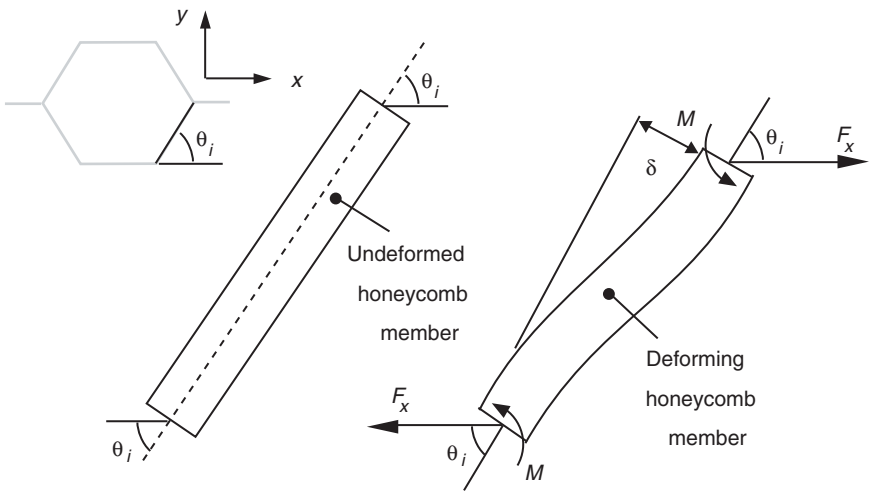

Figure 4. *Wall deformation due to loads in the horizontal direction.*

This simple analysis demonstrates how the material stiffness relates to the stiffness in the longitudinal direction. The same argument can be presented in the y-direction (Gibson and Ashby, 1988):

$$\bar{E}_y^m = E^m \left(\frac{t}{l}\right)^3 \frac{\sin\theta_i}{(1+\cos\theta_i)\cos^2\theta_i}. \tag{7}$$

For the case that the honeycomb has perfectly hexagonal cells (i.e., $\theta_i = \pi/3$)) these equations simplify to:

$$\bar{E}_x^m = \bar{E}_y^m = \frac{4}{\sqrt{3}}\left(\frac{t}{l}\right)^3 \tag{8}$$

It has been shown that this theory works well for global strains up to 20% and $t/l < 1/4$ (Gibson and Ashby, 1988). It should be noted that although the overall or global strains can reach extremely high levels (in some cases, more than 100%), the local strain levels in thin-walled honeycomb are typically well below yield for common engineering materials like aluminum and steel foils. Furthermore, it does not consider amplified deflections due to axial loads that are introduced in the diagonal beams. It is assumed that deformation is purely based on the bending of the diagonal elements. If Equation (6) is inverted, the material stiffness can be determined when the overall stiffness in the x-direction is known from structural tests on a honeycomb structure:

$$E^m = \bar{E}_x^m \left(\frac{l}{t}\right)^3 \frac{\sin^3\theta_i}{\cos\theta_i + 1}. \tag{9}$$

This expression can be altered to account for the case of pressure-adaptive honeycomb where the stiffness is induced solely by the pressure. In that case, the material stiffness is replaced by the pressure-induced material stiffness, E^p, and can be found from:

$$E^p = \bar{E}_x^p \left(\frac{l}{t}\right)^3 \frac{\sin^3\theta_i}{\cos\theta_i + 1} = \bar{E}_y^p \left(\frac{l}{t}\right)^3 \frac{(1+\cos\theta_i)\cos^2\theta_i}{\sin\theta_i}. \tag{10}$$

E^p is a stiffness modulus that maps the structural stiffness of the structure onto the honeycomb cell walls. In other words, the pressure-induced stiffness is implicitly incorporated in the stiffness of the honeycomb walls. If this model is, in turn, used to predict the structural mechanics of a large pressurized honeycomb structure, it reduces the modeling complexity by leaving out the explicit definition of the surface pressures within the honeycomb.

If both material stiffness and pressure-induced stiffness are to be incorporated in an *equivalent* material stiffness is defined according to:

$$E^{eq} = E^m + E^p \tag{11}$$

For a given honeycomb structure of unknown equivalent material stiffness, either the overall stiffness in x-direction or the overall stiffness in y-direction is necessary to determine the equivalent material stiffness. Since E^m can readily be found from material data, E^p needs to be predicted from $\bar{E}_x^p$ or $\bar{E}_y^p$. The subsequent section presents a theory on how to predict those overall stiffness moduli.

Pressure-Induced Stiffness

In the previous section, it was shown how the Young's modulus of the material of ordinary honeycomb can be related to the overall stiffness of a honeycomb block.

In this section, the objective is to determine the principal stiffness moduli of a *pressurized* honeycomb block, $\bar{E}_x^p$ and $\bar{E}_y^p$, respectively.

MODEL SETUP AND ASSUMPTIONS

In order to separate the interaction between the honeycomb and the pouches (which could lead to friction-based resistance to deformation), an energy approach is taken that relates the change in pressurized volume to the mechanical work. Because the total volume is of importance, rather than the deformation of the individual ligaments (or cell walls) the following geometric simplification is proposed. Each cell is represented by a hexagon of rigid walls that are connected to each other by means of frictionless hinges in the corners. The reader can verify that such a structure by itself (not pressurized) does not have any stiffness. Any resistance to deformation therefore stems from the addition of the pressurized volumes inside the honeycomb. For a small thickness-to-length ratio (i.e. $t/l \ll\ll\ll\ll 1$), this approximation yields kinematic relations that are very close to those of actual thin-walled honeycomb.

If Figure 3 is considered, one can easily see that the volume occupied by the pouches is smaller than the total cell volume occupied by all the cells. In this analysis, it is assumed that this ratio remains constant during deformation. Furthermore, this ratio is denoted with ζ and is set to the ratio of a circle inside a perfect hexagon (i.e. $\theta_i = \pi/3$): $\zeta = \sqrt{\pi}/6 \approx 0.91$. It has been experimentally demonstrated that this value is in reality a minimum and that upon deformation the pouch-to-cell volume ratio increases (Vos, 2009). For the stiffness relation that is derived in the subsequent sections, this ratio will appear as a factor that multiplies with the pressure. The choice to fix this parameter has been made to simplify the subsequent analysis. By fixing ζ at its minimum value, a conservative assumption is made about the pressure-induced stiffness.

STRESS–STRAIN RELATION FOR PRESSURIZED HONEYCOMBS

If the pressurized honeycomb is modeled according to a structure of rigid members connected by hinges, then the volume of the incremental section is determined by the honeycomb angle, θ. When an external stress field is applied to the overall structure, the discrete forces on the diagonal members can be deduced. This is schematically shown in Figure 5. The combination of a stress in the x-direction and the y-direction leads to a discrete force, F, on the diagonal member. The magnitude of this force and its direction (φ) can be related to the overall stress according to following relations:

$$\sigma_x = \frac{F\cos\varphi}{l\sin\theta_i}, \tag{12}$$

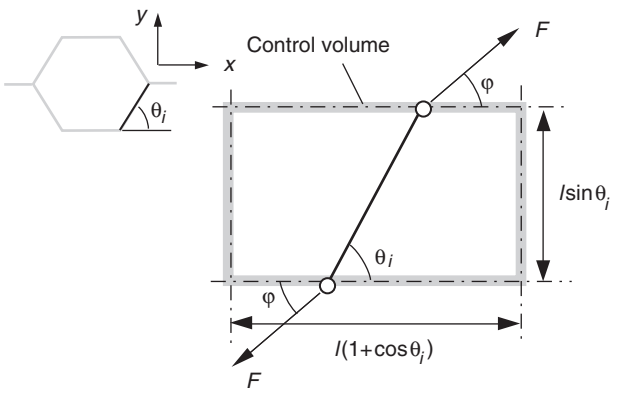

Figure 5. *Forces on incremental section stemming from normal stresses.*

$$\sigma_y = \frac{F\sin\varphi}{l(1+\cos\theta_i)}. \tag{13}$$

Knowing that the control volume, V, of Figure 5 is pressurized, the work that needs to be done in order to alter the volume (denoted as useful work in Rolle, 2005) can be expressed as:

$$W_{\text{use}} = \int_{V_i}^{V} p\,\mathrm{d}V - p_a(V - V_i), \tag{14}$$

where V_i is the initial volume. When the pressure in the cells is kept constant (which is a realistic scenario for the implementation of this structure into an aerospace application) this integral can be evaluated as follows:

$$W_{\text{use}} = (p - p_a)(V - V_i). \tag{15}$$

This useful work, should be balanced by the work done by the external force F over a particular distance, s, aligned with the direction of F:

$$W_{ex} = \int_s F\,\mathrm{d}s. \tag{16}$$

From geometry, the incremental displacement, $\mathrm{d}s$ can be shown to relate to the honeycomb angle, θ, as follows:

$$\mathrm{d}s = -l\sin(\theta - \varphi)\mathrm{d}\theta. \tag{17}$$

Substituting in Equation (16) and integrating between θ_i and θ result in the following expression for the external work:

$$W_{ex} = Fl[\cos(\theta - \varphi) - \cos(\theta_i - \varphi)]. \tag{18}$$

From the balance between external work (Equation (18)) and the useful work (Equation (15)), the relation between the external force, the direction of the force,

and the cell differential pressure (CDP, defined as $\mathrm{CDP} = p - p_a$) can be defined:

$$F = \frac{1}{l}\frac{(p-p_a)(V-V_i)}{\cos(\theta-\varphi)-\cos(\theta_i-\varphi)}, \tag{19}$$

where the volume is calculated according to (Figure 5):

$$V = \zeta l^2 \sin\theta(1+\cos\theta). \tag{20}$$

The initial volume, V_i, can be found by substituting $\theta = \theta_i$ in Equation (20). In case of principal stresses in the x-direction, the angle $\varphi = 0$. Alternatively, when there exist only stresses in the y-direction it follows that $\varphi = \pi/2$. Combining Equation (19) with Equations (12) and (13) results in the following stresses in principal direction:

$$\sigma_x = \frac{1}{l^2\sin\theta_i}\times\frac{(p-p_a)(V-V_i)}{\cos\theta-\cos\theta_i} \tag{21}$$

$$\sigma_y = \frac{1}{l^2(1+\cos\theta_i)}\times\frac{(p-p_a)(V-V_i)}{\sin\theta-\sin\theta_i} \tag{22}$$

The overall strain of the rigid-member honeycomb is related to the honeycomb angle according to:

$$\varepsilon_x = \frac{\cos\theta-\cos\theta_i}{1+\cos\theta_i}, \tag{23}$$

$$\varepsilon_y = \frac{\sin\theta-\sin\theta_i}{\sin\theta_i}. \tag{24}$$

The reader should observe from Equations (21) through (24) that there exists a highly non-linear relationship between stress and strain in the two principal directions. Furthermore, it can be seen that the principal stresses vary linearly with the CDP.

PRESSURE-INDUCED STIFFNESS VARIATION WITH STRAIN

Equations (21)–(24) form the parametric model of the stress–strain relations in principal directions of rigid-member, pressurized honeycomb. Based on these relations, the equivalent Young's moduli in principal direction can be derived. Because these moduli are representative for overall stiffness of the pressurized, rigid-member honeycomb, they are denoted with $\bar{E}_x^p$ and $\bar{E}_y^p$, respectively. They can be found by applying the chain rule in the following fashion:

$$\bar{E}_x^p = \frac{\mathrm{d}\sigma_x}{\mathrm{d}\varepsilon_x} = \frac{\partial\sigma_x}{\partial\theta}\frac{\partial\theta}{\partial\varepsilon_x}, \tag{25}$$

$$\bar{E}_y^p = \frac{\mathrm{d}\sigma_y}{\mathrm{d}\varepsilon_y} = \frac{\partial\sigma_y}{\partial\theta}\frac{\partial\theta}{\partial\varepsilon_y}. \tag{26}$$

Substituting Equations (21) through (24) results in closed-form analytical expressions for $\bar{E}_x^p$ and $\bar{E}_y^p$, respectively. These expressions can easily be obtained by evaluating the partial derivatives in Equations (25) and (26):

$$\bar{E}_x^p = -\frac{p-p_a}{l^2\sin\theta_i}\times\frac{(\cos\theta-\cos\theta_i)\mathrm{d}V/\mathrm{d}\theta+(V-V_i)\sin\theta}{(\cos\theta-\cos\theta_i)^2}\times\frac{1+\cos\theta_i}{\sin\theta} \tag{27}$$

$$\bar{E}_y^p = \frac{p-p_a}{l^2(1+\cos\theta_i)}\times\frac{(\sin\theta-\sin\theta_i)\mathrm{d}V/\mathrm{d}\theta-(V-V_i)\cos\theta}{(\sin\theta-\sin\theta_i)^2}\times\frac{\sin\theta_i}{\cos\theta} \tag{28}$$

Note that $\mathrm{d}V/\mathrm{d}\theta = \zeta l^2(\cos\theta+\cos 2\theta)$ from Equation (20). The dependency of $\bar{E}_x^p$ and $\bar{E}_y^p$ on θ shows that the overall stiffness of the pressurized honeycomb changes during deformation. A graphical representation of the (non-linear) variation of stiffness with strain is shown in Figure 6 for the case when $\theta_i = \pi/3$. This non-linear variation with strain also implies a non-linear relationship between stress and strain. In the following sections, this model will therefore be annotated as the *non-linear* model.

Now, that $\bar{E}_x^p$ and $\bar{E}_y^p$ have been determined, E^p can be calculated with Equation (10). The resulting pressure-induced stiffness is highly non-linear. Adding the material stiffness, E^m, in Equation (1) results in a function for the equivalent material stiffness E^{eq}.

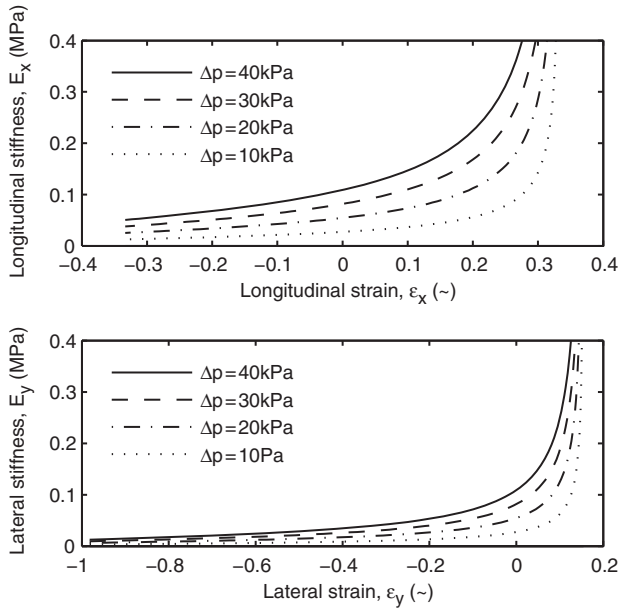

Figure 6. *Stiffness variation with strain at elevated CDPs ($\Delta p = p - p_a$ and $\theta_i = \pi/3$).*

CONSTANT PRESSURE-INDUCED STIFFNESS

In this case, a pressurized honeycomb is considered that consists of perfect hexagonal cells (i.e., $\theta_i = \pi/3$). A constant value of the stiffness may be assumed as long as the predicted stress based on this constant value does not differ more than 5% from the analytical value as calculated by Equations (21) and (22), for the stresses in x- and y-direction, respectively. In that case, the stiffness moduli (Equations (25) and (26)) should be evaluated at $\theta = \theta_i = \pi/3$. Because of mathematical considerations (numerator and denominator are both zero), this results in evaluating the following limits:

$$\lim_{\theta \to \theta_i = \pi/3} \bar{E}_x^p = 3\zeta(p - p_a) \tag{29}$$

$$\lim_{\theta \to \theta_i = \pi/3} \bar{E}_y^p = 3\zeta(p - p_a) \tag{30}$$

These simple expressions demonstrate that when the honeycomb forms perfect hexagonal cells, the stiffness moduli in x- and y-directions are identical. This agrees with CMT for unpressurized honeycomb cells that also display this orthotropic behavior with the same modulus in each principal direction. A constant stiffness modulus implies a linear relationship between stress and strain. In the proceeding sections, this model will therefore be annotated as the *linear* model. Equation (10) can be employed to determine the pressure-induced material stiffness (E^p). In turn, by substituting this in Equation (1) together with the material stiffness, E^m, results in a constant value for the equivalent material stiffness E^{eq}. If it is assumed that for the initial geometry $\theta_i = \pi/3$, then the following equivalent stiffness modulus of the pressurized, flexible-wall honeycomb can be deduced:

$$E^{eq} = E^m + \frac{3\sqrt{3}\zeta}{4}\left(\frac{l}{t}\right)^3 (p - p_a) \tag{31}$$

This equivalent stiffness is used in the FE calculations for a rectangular honeycomb beam in a three-point bend test (sections "EXPERIMENTAL SETUPS AND TESTING PROCEDURES" and "RESULTS AND COMPARISON TO THEORY"). Rather than specifying an individual pouch with pressure forces on each of the boundaries, the structure can now be modeled as ordinary honeycomb, having a stiffness that is proportional to the pressure differential.

EXPERIMENTAL SETUPS AND TESTING PROCEDURES

To investigate the validity of the previously presented models, a series of tests were carried out. In the following three subsections the test articles and testing methods are presented. First, a test is described that compares the stress–strain relations of pressurized rigid-wall honeycomb to the analytic predictions of section "MODELING PRESSURIZED HONEYCOMB". Based on the positive outcome of this test, the stress–strain behavior of pressurized flexible-wall honeycomb is described in the subsequent section and compared to the theory of section "MODELING PRESSURIZED HONEYCOMB". Finally, the assumption of having a constant equivalent material stiffness is tested by comparing the results of a three-point bend test to predictions of a FE approximation based on this assumption.

Rigid-member Pressurized Honeycomb

The honeycomb grid was manufactured out of two-ply Kevlar laminates ($t \approx 0.50$ mm) that had a relatively high-bending stiffness. The hinges were introduced by local carbonization of the matrix structure, which degraded the bending stiffness dramatically. This resulted in a structure with nearly frictionless hinges and approximately rigid walls, similar to the model presented in section "MODELING PRESSURIZED HONEYCOMB". The characteristic wall length of each hexagon face amounted to $l = 20$ mm. In the plane of the honeycomb cells, the outer dimensions in the x- and y-directions of the honeycomb grid were 180×173 mm, respectively. The length of specimen in z-direction measured 290 mm. To be able to distribute a point load over the length of all the cells, c-stiffeners were bonded to the specimen such that they spanned the length of the cells. Each of the 23 cells inhabited a Mylar pouch. All the pouches were subsequently pierced with a hypodermic needle, which were, in turn, connected in series by a rubber tube. By attaching the rubber tube to a pressure variation apparatus on the one end and a pressure sensor on the other end, the pressure in the tube could be controlled and monitored. The pressure sensor connected to a data-acquisition unit that interfaced with Labview. The test specimen was positioned in an MTS858 Mini Bionix II servo hydraulic testing frame (see Figure 7 for details). This machine was equipped with two caul plates between which the specimen was sandwiched. To allow for free lateral contraction of the specimen, all the c-stiffeners were coated with a layer of 51 μm thick Teflease™. In addition, the caul plates were covered in a thin layer of petroleum jelly to ensure minimum friction between the specimen and the machine.

For the longitudinal compression test, the specimen was positioned in the Mini Bionix such that a distributed load could be introduced in the x-direction. Pressure, force, and displacement were recorded during this compression test at a rate of 1 Hz. This test was carried out at 10 different CDPs, starting at 5 kPa and ending at 50 kPa in steps of 5 kPa. For the lateral compression

test, the specimen was rotated 90° and the same test procedure was applied.

Pressurized Aluminum Honeycomb

To investigate the structural properties of pressurized honeycomb, a 130-cell aluminum specimen was fabricated. This was the first test article that combined an aluminum honeycomb structure that could be pressurized such as to alter its stiffness. The tests on this specimen were conducted to see if the analytical models of section "MODELING PRESSURIZED HONEYCOMB" could be applied to predict the mechanics of pressurized honeycomb.

As a base material, Aluminum 1145H19 was chosen with a thickness of 76 μm. The reason for this option was that it had shown good manufacturability properties for the honeycomb in the sense that it allowed for straight folds to be induced by a press-brake. In addition, it had relatively high-yield strength, which was important because it needed to stay in the elastic realm while loaded. The aluminum sheets were cut, folded, and bonded together using Hysol 9412. The face length of a characteristic cell measured $l = 15$ mm. Due to imperfect manufacturing techniques using the press brake, the anticipated fold angle of 60° was not achieved. This was mainly due to the spring back of the material. The finished specimen had an average honeycomb angle of only 53°. Using Equations (6) and (7), resulted in the following stiffness values: $\bar{E}_x^m = 28.9$ kPa and $\bar{E}_y^m = 12.6$ kPa, respectively.

The lateral compression test was the first test to be carried out. To be able to provide relatively constant distributed load over the top and bottom surfaces of the test article, two thick (8 cm) compression boards were fabricated. These boards were made as a sandwich where a Styrofoam core was bonded to two stiff plastic plates on either side. The top board was connected to a 20-mm thick aluminum plate, which in turn connected to the force transducer on the Instron machine *via* a swivel joint. The bottom board was connected to a 25-mm thick aluminum plate, which was then bolted to the Instron machine. The test article was positioned in between the upper and lower boards. Petroleum jelly was applied between the surface of the test article and the board surface. This enabled the test article to expand perpendicular to the direction of applied load with minimum friction. The Instron 3345 was slightly modified to geometrically allow for such a large test article. The arm between the thread rod inside the machine and the force transducer was made twice as long by means of an aluminum extension. Since the Instron 3345 was rated at a maximum load of 5 kN, it was decided that due to the doubling of the moment arm, a new limit of 2.5 kN needed to be enforced to ensure the integrity of the machine (Figure 8).

The measurement and control of the Instron 3345 were carried out by using the software package Bluehill 2. The specimen was compressed at a rate of 0.1% strain per second. A maximum down stroke of 15% strain was prescribed such as to avoid plastic deformation in the aluminum ligaments (this was detected in an earlier test when the honeycomb specimen was strained in lateral compression up to 20%). During the experiment the force was measured at a rate of 1 Hz. In addition, the pressure was controlled with the aforementioned pressure apparatus and was monitored in Labview by means of a pressure transducer. Pressure measurements were taken simultaneously with the force measurements at a rate of 1 Hz.

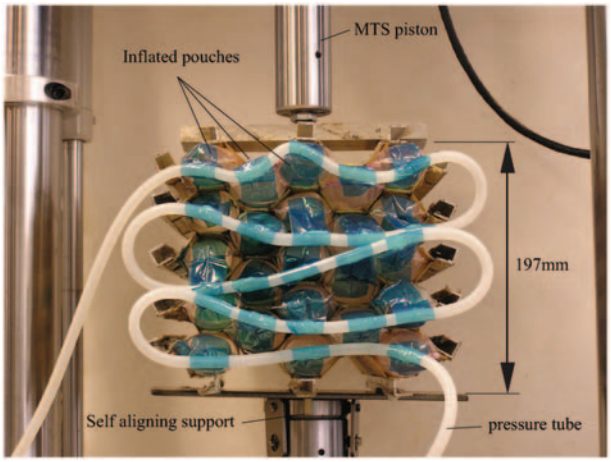

Figure 7. *Pressurized rigid-wall honeycomb in MTS machine (lateral compression test).*

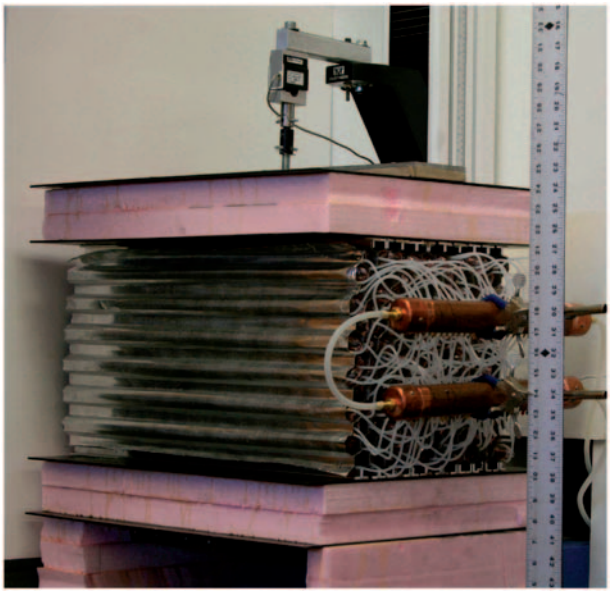

Figure 8. *Experimental test setup of pressurized flexible-wall honeycomb in Instron 3345 (longitudinal compression).*

To allow for hysteresis analysis, the test was carried out in a loop, where data were taken in the upstroke (0–15% strain) and downstroke (15–0% strain). Four tests were carried out at target pressures of 10, 20, 30, and 40 kPa. Pressure, force, and displacement were recorded. A post-processing code in Matlab was written that read the experimental results, translated the force/displacement measurements to average stress/strain measurements based on the geometry of the test article.

Three-Point Bend Test

The previously described experiments were designed to capture the stress–strain behavior of pressure-adaptive honeycomb. From the results of these tests, an equivalent material stiffness could be deduced that could be used in the finite element analysis (FEA). To test if this method would result in accurate predictions for the mechanics of pressure-adaptive honeycomb in an application, a three-point bend test was carried out. To that extent, a 145-cell beam shaped test article was employed.

It proved challenging to properly align all the corrugated sheets on the rectangular (145-cell) specimen. The reader can understand that due to imperfect manufacturing techniques, not all the folds in the corrugated sheets were exactly parallel to one another. This resulted in slightly irregular sides in the plane of the honeycomb cells. Because of the high-aspect ratio of the cells themselves, this was not perceived to have an adverse effect on any of the measurements that would be acquired by subjecting this test article to a load as the manufacturing imperfections were typically under 2 mm from one end to another.

To accommodate this rather large test article, a frame was built that could be mounted to the base of the Instron machine. It was anticipated that the forces in this test would not be as high as during the compressive and tensile tests on the 130-cell specimen. It was therefore decided to extend the arm of the instron out even further such that the force could be applied in the center of the test article. To simplify the test setup, the test rig was built such that the Instron could pull on the base plate and hence induce curvature in the beam. A wooden frame was built with two steel pins that provided the simply supported boundary conditions. The test frame was rigidly attached to the base of the Instron while the test article was hung from the Instron's force transducer. Figure 9(a) shows the experimental setup for this three-point bend test. By displacing the force transducer upwards bending was introduced in the test article. In Figure 9, the experimental setup is schematically shown for clarity.

RESULTS AND COMPARISON TO THEORY

The subsequent sections present the results of the experimental tests on the rigid-member honeycomb, the flexible-wall honeycomb, and the honeycomb beam element, respectively. The experimental results are compared to the predicted results based on the models presented in section "MODELING PRESSURIZED HONEYCOMB".

To quantify the error and correlation between the prediction and the experiment, the error, e_i, is calculated at each measured data point, i according to:

$$e_i = \frac{F_i}{S\Delta p_i} - \frac{\sigma_i^{\text{predicted}}}{\Delta p_{\text{average}}} \tag{32}$$

where $\sigma_i^{\text{predicted}}$ can either be substituted by the linear or the non-linear prediction of the normal stress at a given strain value. The term $F_i/S/\Delta p_i$ is the measured normal stress F_i/S, divided by the pressure differential, Δp. This yields the error to be a dimensionless value expressed as a fraction of the CDP. The average CDP in the second

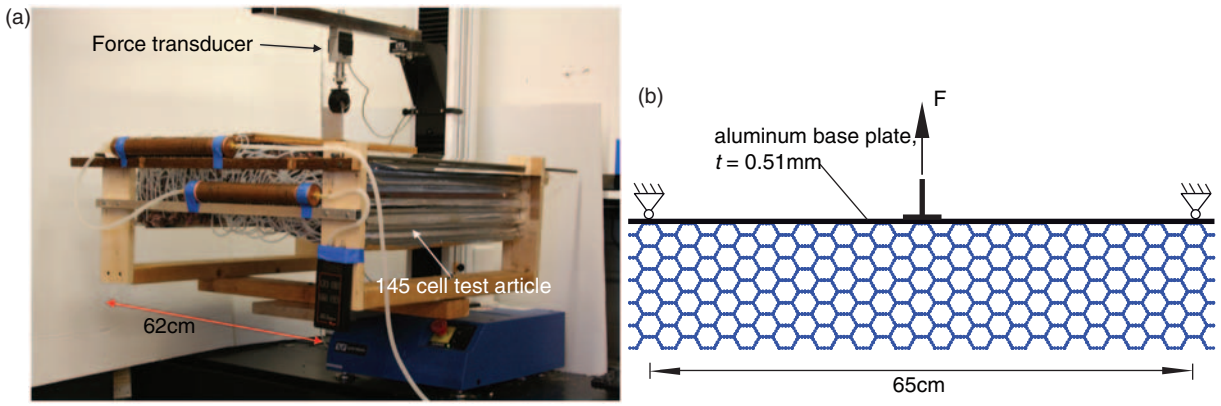

Figure 9. *Three-point bend test. (a) Experimental test setup. (b) Schematic representation.*

term, $\Delta p_{\text{average}} = \frac{1}{N}\sum_{i=1}^{N} p_i$. The root-mean-square (RMS) of the error is obtained from:

$$\text{RMS} = \sqrt{\frac{\sum_{i=1}^{N} e_i^2}{N}} \tag{33}$$

The RMS quantifies the overall error in stress prediction as a fraction of the CDP. Finally, Pearson's product moment correlation coefficient, R^2 is determined as follows:

$$R^2 = 1 - \frac{\text{Var}(e)}{\text{Var}(\frac{F}{S\Delta p})} \tag{34}$$

In the succeeding subsections, the RMS and R^2 values are used to quantify the prediction capability of the non-linear and linear stress–strain models.

Rigid-Member Pressurized Honeycomb

The rigid-member honeycomb tests were carried out to see how well the linear and non-linear analytical models predicted the actual stress–strain behavior of a honeycomb structure that relied solely on pressure for structural stiffness. It is of interest to see whether the pressure-induced stiffness can be properly captured by one or both of these models.

In total, 20 experiments were carried out (10 in each direction). A selection of the test results of the compressive tests in longitudinal and lateral direction are displayed in Figure 10(a) and (b), respectively. The normal stress is displayed in relation to the normal strain. The experimental results are compared to the non-linear stress–strain model (Equations (21) and (23) in longitudinal direction and Equations (22) and (24) in lateral direction) and the linear stress–strain model (with constant stiffness, E^p, as in Equation (31)). It might be observed that the curves do not start at the origin. This is because the specimen was loaded with a 10 N pre-force before the testing started. At this force the displacement was zeroed. The displacement-induced by this small initial load was estimated by dividing the pre-force by the average slope of the experimental curve over the first 2% of compressive strain. At lower pressures, this resulted in a higher offset in strain than at higher pressures, as can be seen from the difference between the individual plots in Figure 10(a) and (b).

A quantification of the RMS and correlation coefficient, R^2, are presented in Figure 11(a) and (b). Note that these coefficients only apply over the measured strain range of 12%. Generally, a good correlation exists between the non-linear analytical model and the experimental results in longitudinal direction. Correlation between the non-linear model and the experimental data is possibly even better in the lateral direction than in the longitudinal direction. The correlation was rather poor at low CDPs (<10 kPa). It must be noted, however, that during this experiment, the stiffness of the honeycomb structure itself contributed to the total stiffness of the system. Therefore, in this experiment, the pure pressure-induced stiffness was augmented by the residual stiffness in the specimen. However, as CDP increased, the relative stiffness of the honeycomb structure diminished and the correlation between prediction and experiment

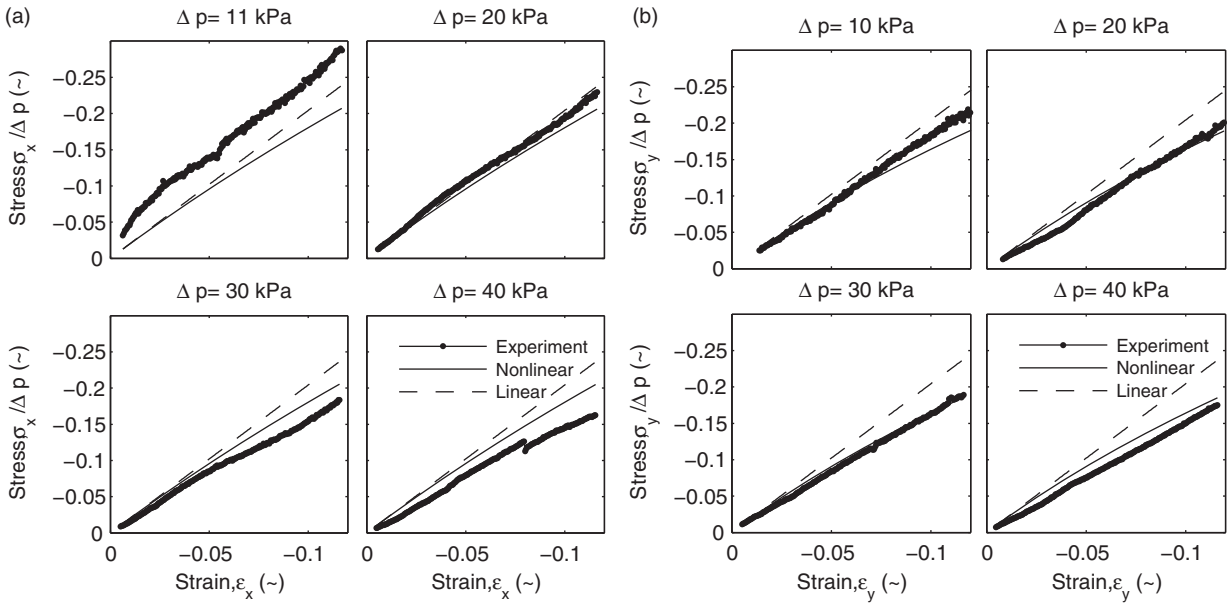

Figure 10. *Experimental and analytical results for compression test of rigid-member pressurized honeycomb. (a) Longitudinal compression. (b) Lateral compression.*

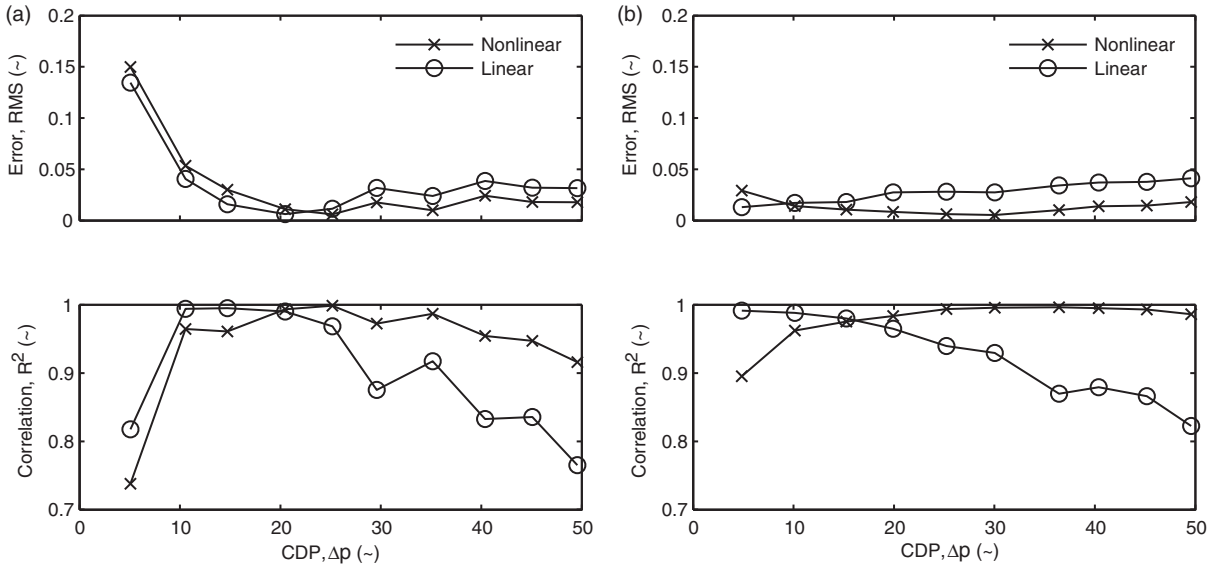

Figure 11. *RMS and correlation for pressurized rigid-wall honeycomb. (a) Longitudinal compression. (b) Lateral compression.*

improved. At a CDP of 40 kPa, the experimental results showed lower stress values beyond 7% of strain than the predicted values. The linearized model generally showed good correlation at low strains but its error with respect to the experimental data increased with strain.

From these experiments, it was concluded that the non-linear model could properly predict the stress–strain behavior of the pressurized honeycomb over a compressive strain of 12%. This was a strong indication that the non-linear model could be used with confidence to predict the stiffness of pressurized honeycomb as a function of the CDP.

Pressurized Aluminum Honeycomb

The results presented in the previous sections demonstrated that the analytical model for pressurized honeycomb could be used to predict the stress–strain behavior of rigid-member honeycomb. In other words, the pressure-induced stiffness could be predicted at least for compressive strains up to 12%. In this section, it is investigated if the expansion of this model to metallic honeycomb structures can also be used to predict the stress–strain relation of pressurized honeycomb. It is of interest to see if the added material stiffness can also be captured by the non-linear and linear analytical models. Furthermore, it is to be seen whether the slightly different kinematics (wall bending rather than hinging) is not prohibitive in predicting the overall stress–strain behavior.

The limiting factor in this experiment was the maximum force that the Instron could provide (2.5 kN). Based on preliminary experiments at 40 kPa, the resulting maximum compressive strain in longitudinal direction at this force was set at 12.5%. In the case of lateral compression, the maximum compressive strain amounted to 16%. In Figure 12(a) and (b), the experimental stress–strain data are presented in longitudinal and lateral directions, respectively. In addition, the non-linear prediction based on the non-linear equivalent material stiffness (as explained in section "MODELING PRESSURIZED HONEYCOMB") as well as the linear prediction is presented (with a constant equivalent stiffness as in Equation 31).

It can be observed that for both longitudinal and lateral compressions, the non-linear model gives an excellent prediction of the global stress–strain behavior. Small deviations from the predictions were attributed to the flexibility of the honeycomb walls that led to different kinematics than the rigid-wall honeycombs which the analytic models were based on. It can also be observed that at particular higher CDPs, the experimental curves show some non-linearity. This is in line with the predictions of the non-linear model. It is expected that when the measurement range of strains would be increased, this non-linear behavior would become even more pronounced. The RMS and correlation coefficients are presented in Tables 1 and 2. It can be seen that the correlation between non-linear prediction and experimental results remained relatively high ($R^2 \geq 0.98$) over the range of measured strains and the four different CDPs. The correlation with the linear model (assuming constant equivalent stiffness) was rather bad for the lateral compression case.

Based on the results presented in this section, along with results shown for the rigid-wall compression test, it might be concluded that the non-linear model can provide a good estimate of the overall-stress–strain behavior of a pressurized honeycomb structure. It should be noted that this is based on a limited number of

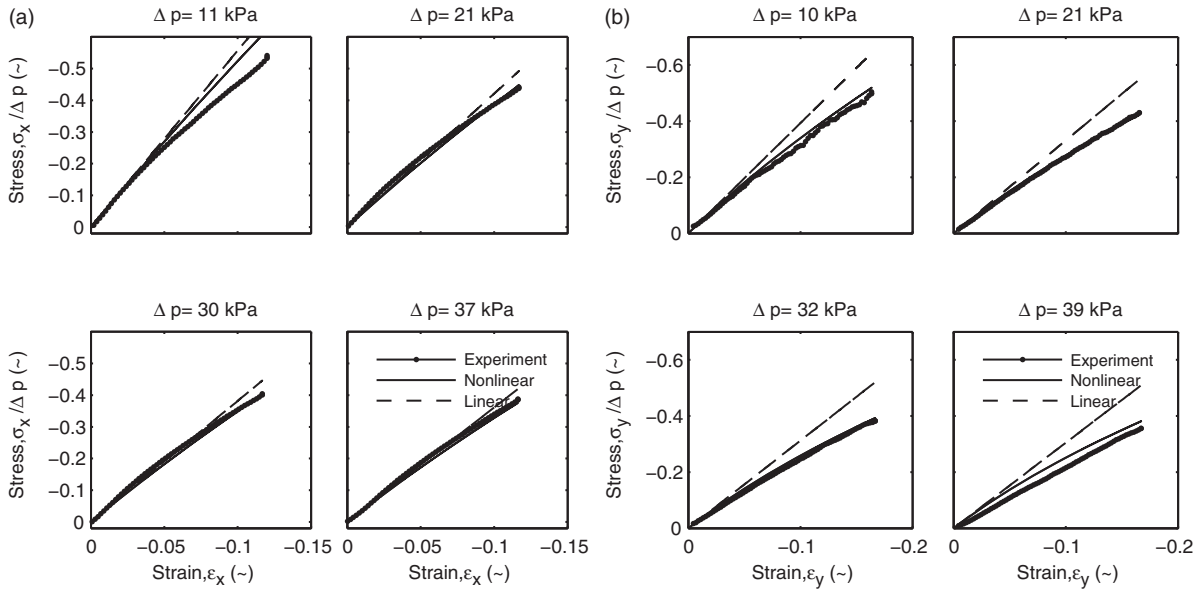

Figure 12. *Experimental and analytical results for compression test of aluminum pressurized honeycomb. (a) Longitudinal compression. (b) Lateral compression.*

Table 1. Error and correlation coefficients for longitudinal compression test of pressurized aluminum honeycomb.

	Non-linear		Linear	
CDP (kPa)	RMS	R^2	RMS	R^2
11	0.034	0.96	0.050	0.91
21	0.009	0.99	0.017	0.97
30	0.008	1.00	0.014	0.98
37	0.008	1.00	0.010	0.99

Table 2. Error and correlation coefficients for lateral compression test of pressurized aluminum honeycomb.

	Non-linear		Linear	
CDP (kPa)	RMS	R^2	RMS	R^2
10	0.013	0.99	0.113	0.89
21	0.004	1.00	0.073	0.91
32	0.007	1.00	0.071	0.87
39	0.020	1.00	0.080	0.84

preliminary tests and in order to validate the model, more tests are required. By the same token, the linear model shows much more deviation and should only be used to predict stress–strain behavior for very small overall strains (on the order of 1%).

Three-Point Bend Test

The longitudinal and lateral compression tests were used to establish a relationship between the equivalent material stiffness of the honeycomb and the CDP. To test if such an empirically obtained relationship could be useful in a more complex application of pressure-adaptive honeycomb, a three-point bend test was carried out. A point load was distributed over a small area around the center of the test article (Figure 9). This force introduced a curvature in the beam, which was simply supported. A simulation of this experiment was conducted by using a FEA of the test article and the same loading and boundary conditions as during the experiment. The FEA with equivalent stiffness (E^{eq}) based on the linearization of the analytical model was investigated. The results of the experiment and FEA are shown in Figure 13.

From Figure 13, it can be observed that the correlation of the experimental results to the FEA-generated results is very good. From these experiments, it can be concluded that the FEA with the linear analytical model and the subsequent equivalent stiffness calculation leads to a good prediction of the overall mechanics of pressure-adaptive honeycomb for small deformations. Whether also large deformations can be predicted using this theory cannot be proven from this simple experiment. It is likely that larger deformations require the more accurate non-linear model to include the change in pressure-induced stiffness that is seen at higher strains.

CONCLUSIONS

An analytical model to predict the stress-strain relations of pressure–adaptive honeycomb has been

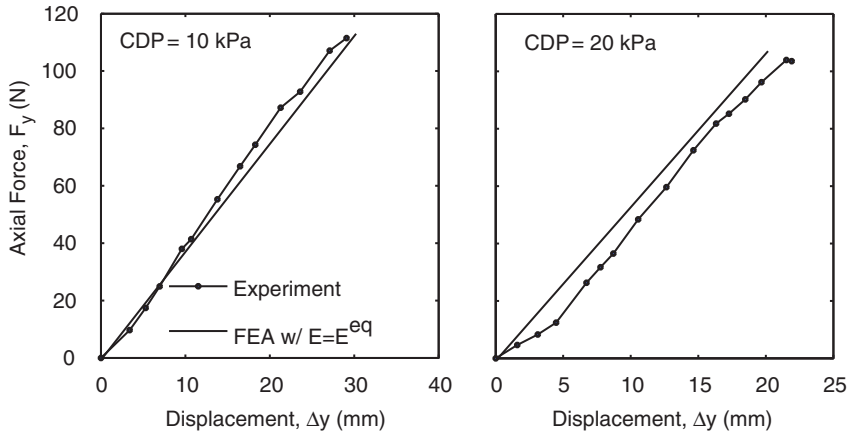

Figure 13. *Experimental and FEA results of three-point bend test.*

presented. The pressure-induced stiffness was compared against experimental results on a rigid-member honeycomb specimen and showed good correlations up to 15% compressive strains at cell-differential levels of 40 kPa. Subsequent tests on a 130-cell aluminum specimen demonstrated that the material-induced and pressure-induced stiffness show good correlation to the predictions of the analytical model. Based on the analytical model an equivalent Young's modulus was defined for the honeycomb walls that incorporated the material-induced stiffness as well as the pressure-induced stiffness. This equivalent stiffness was used in a FE approximation of a 145-cell honeycomb beam element, without explicit modeling of the cell differential pressure or the pouches. Predicted results of the FEA for a three-point bend test showed good correlation to experimental results for small deformations.

NOMENCLATURE

e	error
E	Young's modulus (N/m^2)
E	overall stiffness modulus (N/m^2)
F	force (N)
I	second moment of area (m^4)
l	wall length (m)
N	number of data points
p	pressure (N/m^2)
R^2	Pearson's product-moment correlation coefficient
S	surface area (m^2)
t	wall thickness (m)
V	volume (m^3)

Greek Symbols

ε	strain
δ	deformation distance (m)
θ	honeycomb angle (deg)
σ	stress (N/m^2)

Subscripts and Superscripts

eq	equivalent
i	initial or index
m	material-induced
p	pressure-induced
x	longitudinal direction
y	lateral direction
z	direction perpendicular to cell-plane

Abbreviations

CDP	cell differential pressure = Δp (N/m^2)
CMT	cellular material theory
FE	finite element
RMS	root mean square of the error
SMA	shape memory alloy

ACKNOWLEDGMENTS

The authors wish to acknowledge the generous support of the University of Kansas Transportation Research Institute (TRI) and the Aerospace Engineering Department for funding this research. In addition, the authors wish to acknowledge the support from Professor Karan S. Surana, Mechanical Engineering Department, University of Kansas, for providing the FE program FINESSE to perform the FE computations in this study. The authors would also like to recognize Ms. Lauren Kerth, Mr. Thomas Stastny, and Mr. Ryan Barnhart for their tireless efforts in assisting fabricating the test articles.

REFERENCES

Anon. 2009. *Comparison of EAPs with Other Actuator Technologies*. Available at: ndeaa.jpl.nasa.gov/nasa-nde/lommas/eap/, SRI International and DARPA (accessed May 30, 2009).

Atli, B. and Gandhi, F. 2008. ''Energy Absorption of Cellular Honeycombs with Various Cell Angles under In-Plane Compressive Loading,'' In: *49th AIAA/ASME/ASCE/AHS/ASC Structures, Structural Dynamics, and Materials Conference*, Schaumburg, IL.

Bowman, J., Sanders, B., Cannon, B., Kudva, J., Joshi, S. and Weisshaar, T. 2007. ''Development of Next Generation Morphing Aircraft Structures,'' In: *48th AIAA/ASME/ASCE/AHS/ASC Structures, Structural Dynamics, and Materials Conference,* AIAA Paper 2007-1707, Honolulu, HI.

Bubert, E.A., Woods, B.K.S., Lee, K., Kothera, C.S. and Wereley, N.M. 2010. ''Design and Fabrication of a Passive 1D Morphing Aircraft Skin,'' *Journal of Intelligent Materials Systems and Structures*, 21:1699–1717.

Cadogan, D., Smith, T., Uhelsky, F. and MacKusick, M. 2004. ''Morphing Inflatable Wing Development for Compact Package Unmanned Aerial Vehicles,'' In: *45th AIAA/ASME/ASCE/AHS/ASC Structures, Structural Dynamics and Materials Conference,* AIAA 2004-1807, Palm Springs, CA.

Calkins, F.T. and Butler, G.W. 2006. ''Variable Geometry Chevrons for Jet Noise Reduction,'' In: *12th AIAA/CEAS Aeroacoustics Conference,* AIAA Paper 2006-2546, Cambridge, MA.

DeCamp, R.W. and Hardy, R. 1984. ''Mission Adaptive Wing Advanced Research Concepts,'' In: *A Collection of Technical Papers (AIAA Atmospheric Flight Mechanics Conference)*, American Institute of Aeronautics and Astronautics, Washington, D.C., pp. 465–470.

Flanagan, J.S., Strutzenberg, R.C., Myers, R.B. and Rodrian, J.E. 2007. ''Development and Flight Testing of a Morphing Aircraft, the NextGen MFX-1,'' In: *48th AIAA/ASME/ASCE/AHS/ASC Structures, Structural Dynamics, and Materials Conference,* AIAA Paper 2007-1707, Honolulu, HI.

Gibson, L.J. and Ashby, M.F. 1988. *Cellular Solids, Structure and Properties*, 1st edn, Cambridge University Press, Cambridge.

Gould, D.K. 1981. ''Mission Adaptive Wing Flight Demonstration Program,'' In: *SAE Aerospace Congress & Exposition,* SAE-811035, Anaheim, CA.

Ivanco, T.G., Scott, R.C., Love, M.H., Zink, S. and Weisshaar, T.A. 2007. ''Validation of the Lockheed Martin Morphing Concept with Wind Tunnel Testing,'' In: *48th AIAA/ASME/ASCE/AHS/ASC Structures, Structural Dynamics, and Materials Conference,* AIAA Paper 2007-2235, Honolulu, HI.

Khire, R.A., Dessel, S.V., Messac, A. and Mullur, A.A. 2006. ''Study of a Honeycomb-Type Rigidified Inflatable Structure for Housing,'' *Journal of Structural Engineering*, 132:1664–1672.

Lewis, G.E., Thomasson, R.E. and Nelson, D.W. 1990. *Wing Lift/Drag Optimization System,* United States Patent 4,899,284, 6 February.

Love, M., Zink, P., Stroud, R., Bye, D., Rizk, S. and White, D. 2007. ''Demonstration of Morphing Technology through Ground and Wind Tunnel Tests,'' In: *48th AIAA/ASME/ASCE/AHS/ASC Structures, Structural Dynamics, and Materials Conference,* AIAA Paper 2007-1729, Honolulu, HI.

Martin, C.A., Hallam, B.J., Flanagan, J.S. and Bartley-Cho, J. 2004. ''Design, Fabrication, and Testing of a Scaled Wind Tunnel Model for the Smart Wing Project,'' *Journal of Intelligent Material Systems and Structures*, 15:269–278.

Norris, R.K. and Pulliam, W.J. 2009. ''Historical Perspective on Inflatable Wing Structures,'' In: *50th AIAA/ASME/ASCE/AHS/ASC Structures, Structural Dynamics, and Materials Conference,* Palm Springs, CA.

Olympio, K.R. and Gandhi, F. 2010. ''Zero Poissons Ratio Cellular Honeycombs for Flex Skins Undergoing One-Dimensional Morphing,'' *Journal of Intelligent Material Systems and Structures*, 21:1719–1735.

Powers, S.G. and Webb, L.D. 1997. *Flight Wing Surface Pressure and Boundary-Layer Data Report from the F-111 Smooth Variable-Camber Supercritical Mission Adaptive Wing*, Technical report, NASA Technical Memorandum 4789, June.

Reinhard, A., To, F.E., Ramseier, O. and Kammer, R. 2001. *Adaptive Pneumatic Wing for Fixed Wing Aircraft,* United States Patent 6,199,796B1, 13 March.

Rolle, K.C. 2005. *Thermodynamics and Heat Power*, 6th edn, Pearson Prentice Hall, Upper Saddle River, NJ.

Sanders, B., Cowan, D. and Scherer, L. 2004. ''Aerodynamic Performance of the Smart Wing Control Effectors,'' *Journal of Intelligent Material Systems and Structures*, 15:293–303.

Shaw, J.A., Churchill, C., Grummon, D., Triantafyllidis, N., Michailidis, P. and Foltz, J. 2007. ''Shape Memory Alloy Honeycombs: Experiments and Simulation,'' In: *48th AIAA/ASME/ASCE/AHS/ASC Structures, Structural Dynamics, and Materials Conference*, Honolulu, HI.

Vos, R. 2009. ''Mechanics and Applications of Pressure Adaptive Honeycomb,'' PhD thesis, University of Kansas, Department of Aerospace Engineering, Lawrence, KS, Septemeber.

Vos, R. and Barrett, R. 2010. ''Pressure Adaptive Honeycomb: A Novel Concept for Morphing Aircraft Structures,'' In: Grant, I. (ed.), In: *Proceedings of the 27th International Congress of the Aeronautical Sciences*, ICAS, ICAS, Nice, France, September.

Woods, B., Bubert, E., Kothera, K. and Wereley, N. 2008. ''Design and Testing of a Biologically Inspired Pneumatic Trailing Edge Flap System,'' In: *49th AIAA/ASME/ASCE/AHS/ASC Structures, Structural Dynamics, and Materials Conference,* AIAA, Schaumburg, IL.